Co-published by
Institute of Fluid-Flow Machinery
Polish Academy of Sciences
Committee on Thermodynamics and Combustion
Polish Academy of Sciences

http://www.imp.gda.pl/archives-of-thermodynamics/

Application of machine learning for reconstruction of multiphase fluid structure measured by a capacitance multi-electrode sensor

Remigiusz Ornowski[a,b], Marcin Lackowski[a], Roman Kwidzinski[a*]

[a]Institute of Fluid Flow Machinery, Polish Academy of Sciences, Heat Transfer Department, Fiszera 14, 80-231 Gdańsk, Poland
[b]TERCJA Measuring and Computer Systems, Dywizjonu 303 5B/24, 80-462 Gdańsk, Poland
*Corresponding author email: roman.kwidzinski@imp.gda.pl

Received: 10.06.2024; revised: 19.08.2024; accepted: 08.10.2024

Abstract

Non-invasive real-time measurements of phase content in the reservoir fluid are highly advantageous in the oil and gas industry and remain a current research topic. The paper presents an innovative, self-designed multi-electrode capacitance meter intended for detecting multiphase flow patterns in a low-permittivity medium, such as the reservoir fluid. The capacitance sensor is built with delta-sigma charge modulators capacitance-to-digital converters. Machine learning is applied to convert the capacitance measurements into a tomographic image of the flow pattern. At present, the meter is built with eight electrodes. It is shown that the measurements are repeatable and have a good signal-to-noise ratio. The implemented neural network is capable of correctly reconstructing the tomographic images for a test tube filled with reservoir fluid and placed in various locations inside the test section.

Keywords: Electrical capacitance tomography; Multiphase reservoir flow; Neural networks; Machine learning; Deep learning

Vol. 45(2024), No. 4, 5–12; doi: 10.24425/ather.2024.151993

Cite this manuscript as: Ornowski, R., Lackowski, M., & Kwidzinski, R. (2024). Application of machine learning for reconstruction of multiphase fluid structure measured by capacitance multi-electrode sensor. *Archives of Thermodynamics*, 45(4), 5–12.

1. Introduction

The extraction of hydrocarbons by well drilling is accompanied by tests of the physical properties of the reservoir fluid, which are performed both during the testing of a new well and during the field production phase. One of the important parameters determined during well testing and productivity monitoring is the phase composition of the reservoir fluid. The phase composition significantly influences the technique that can be used for measuring the fluid flow rate. In the oil (petroleum) and gas industry, processed reservoir fluids are mixtures that in addition to hydrocarbons include water (frequently with dissolved salts) and non-condensable gases (like hydrogen sulfide) [1]. The hydrocarbons form a mixture that may be a liquid, gas or two-phase medium. Hydrocarbon liquid is typically crude oil, while dominating hydrocarbon gases are methane and butane (commonly known as natural gas). Natural gas can be dissolved (partially or completely) in the liquid phase and the amount of dissolved and free gases in the reservoir fluid strongly depends on the fluid pressure and temperature. Under certain thermodynamic conditions, heavy hydrocarbons (paraffin) and asphalts present in the reservoir fluid may solidify.

The traditional and most common method in oil and gas exploration for measuring the phase composition of the reservoir fluid involves the use of a separator enabling the measurement of each phase separately. This method is expensive and requires ongoing maintenance by qualified personnel. Due to the dimensions of the separator, it also requires considerable space, which

Nomenclature

Greek symbols

ε_r – relative permittivity

Abbreviations and Acronyms

ECT – electrical capacitance tomography
fF – femtofarad (10^{-15} F)
FPGA – field-programmable gate array
GVF – gas volume fraction
MFMS – multiphase flow metering systems
WLR – water-in-liquid ratio

may be a problem on offshore drilling platforms. Measurements acquired with this method have low time resolution due to the high inertia of the separator operation but they offer high measurement accuracy for quasi-steady flows. This is because only single-phase flows are measured, for which high accuracy commercial flowmeters are readily available.

The development of electronics and computers in the 1980s resulted in intensified research on the direct measurement of multiphase flow rate, without prior phase separation. In the 1990s, the first multiphase flow metering systems (MFMS) appeared commercially that attracted the interest of the oil & gas industry [2, 3]. The usefulness of such systems has been appreciated in the event of depletion of rich fields and the need to exploit less efficient and less accessible fields that were previously considered unprofitable. The use of MFMS instead of an expensive measurement separator offers a reduction in production costs on such marginal fields. MFMS also enable monitoring of a well production continuously and in real time.

Measuring the volumetric flow rate of a multiphase medium requires determining the volumetric (void) fraction and velocity for each phase. These local quantities determine the flow pattern (structure) in the test cross-section or volume of the flow channel for the pressure and temperature conditions prevailing there. The flow velocities of individual phases may be the same but they are often different (so-called slip). Therefore, a volumetric MFMS most often consists of a sensor measuring the void fraction and a module measuring velocity. To determine the mass flow rate, it is also necessary to measure or evaluate the density of each phase [4, 5].

Available information shows that MFMS are or were offered for the oil & gas industry by several companies. Their design details are often protected by the manufacturers and sometimes even their basic principles of operation are concealed [6]. One of the commercially popular and elaborated multiphase flow meters is marketed under the trademark Roxar 2600 [7]. The basic Roxar model uses impedance measurement to determine phase content and velocity. The velocity is determined based on the cross-correlation of measurements in two planes (flow cross-sections). In the more advanced models, a Venturi tube is added to measure differential pressure and a gamma radiation source (Cesium 137) to measure density. As additional modules, a salinity sensor (for water-dominated flows) and an acoustic sensor for sand monitoring are also available. Roxar 2600 MPFM can be used in three-phase oil, water and gas flows, in the full range of values (from 0% to 100%) of water-in-liquid ratio (WLR) and gas volume fraction (GVF). Under certain conditions, the lowest flowrate measurement uncertainty is 5% for gas, 3% for liquid phase and 2% for WLR [7].

The multiphase flow sensor of the Roxar meter consists of two sets of plate electrodes flush-mounted on the inner wall of the vertical test section. The lower (downstream) set contains six electrodes with a height comparable to the diameter of the test section. Their width is similar to the spaces between them. The upper set consists of two electrodes placed opposite to each other, with the same height as in the lower set and a width covering a segment of a circle (approx. 70–90°). Depending on the electrical properties of the fluid, the same electrodes are used to measure capacitance (when the fluid is dielectric) or conductivity [6]. The measurement in the lower set is rotational and at a time only one electrode is active and the other five are passive. The rotation in the measurement means that the source voltage is switched at equal time intervals from the active electrode to the next (neighbouring) one. According to the manufacturer, processing of the sensor signals allows the determination of the volume occupied by large gas bubbles or slugs and the volume of the dispersed phase in a homogeneous liquid-gas mixture with small bubbles. For large bubbles/slugs, their deviation from the central flow axis is detected. The measurements are also sensitive to the near-wall flow composition. The time of a single measurement is short enough to determine the velocity of large bubbles and the dispersed phase separately. The continuous phase can be either oil or water, and the instrument automatically detects which liquid is present at a given moment.

Non-invasive, fast-response and continuous methods for measuring phase content continuously and in real time remain a current research topic. Particular attention is paid to improving measurement accuracy, extending the measurement range and reliably recognizing multiphase flow structures. This work focuses on the tomographic method using measurements of the electrical capacitance of a multiphase medium. Basic information on multi-electrode capacitive phase content meters can be found, for example, in [8, 9].

Capacitance measurements acquired by tomographic meters can be used to reconstruct the multiphase flow patterns from permittivity distribution, which is equivalent to the spatial distribution of phases in the tested flow domain. An algorithm suitable for this task can be derived considering a set of equations describing the relation between the capacitance (c) and the permittivity (ε). Assuming linear approximation, the change in capacitance (Δc) vector can be related to the changes of permittivity ($\Delta\varepsilon$) according to the equation $\Delta c = S\Delta\varepsilon$, where S is the sensitivity matrix of the transducer [10]. Determining the permittivity from capacitance measurements, known as an inverse problem, can be formally treated as calculating the inverse of the sensitivity matrix (S). However, the problem is ill-posed and ill-conditioned, that is there is no unique solution of the equation

$\Delta c = S\Delta\varepsilon$, and small changes in c (e.g. due to measurement noise) can result in great discrepancies in ε [11]. Therefore, computing the inverse S is a challenging task for which many solution methods have been proposed, among which two classes can be distinguished: direct and iterative. Direct methods include for example linear back-projection, singular value decomposition, and Tikhonov regularization. Examples of the iterative algorithms are Newton–Raphson and iterative Tikhonov methods, Landweber iteration or other steepest descent methods [10].

Apart from the above direct and iterative algorithms, unconventional reconstruction methods based on machine learning have been developed. Nooralahiyan et al. [12] were among the pioneers of using an artificial neural network for solving the inverse image reconstruction problem. Their paper describes the basic principles of an artificial neuron, the multilayer perceptron network and the back-propagation training algorithm, applied in real-time to electrical capacitance tomography (ECT) measurement of multicomponent flows with small (gas/oil) and large (water/oil) difference in permittivity. Later, Marashdeh et al. [13], used a multilayer feed-forward neural network combined with an analog Hopfield field network for solving the nonliner inverse problem. At the same time, Flores et al. [14] investigated the application of neural networks in ECT used in the oil industry. Imaging using the least squares support vector machine (LSSVM) with a self-adaptive particle swarm optimization algorithm was proposed by Chen et al. [15]. On the other hand, Wang et al. [16] studied multiphase flow monitoring by combining the LSSVM with a bacterial colony chemotaxis algorithm. A three-layer feed-forward neural network with radial basis function activation was used by Chen et al. [17] to reconstruct the permittivity distribution from the measured capacitance. Xu et al. [18] proposed a convolutional neural network to predict the oil flow rate, gas flow rate and gas void fraction from measurements with dual ECT sensors and a Venturi tube. A brief overview of other machine learning-based methods can be found in [11].

Based on an own-design unique multi-electrode capacitance meter and machine learning, this article describes the application of tomographic image reconstruction of a low-permittivity material. Reservoir fluid was used as an example of such material. The capacitance sensor is a novel construction built with eight ΔΣ charge modulators capacitance-to-digital converters (CDC).

2. Multi-electrode capacitance sensor

Electrical capacitance tomography is based on measurements of electrical capacitance between electrodes placed around the measured object. In the case of measurements on pipes [9], a set of electrodes is most often used in the form of identical thin plates, distributed evenly around the outer circumference of a non-conductive pipe. Mutual capacitances between individual electrodes are measured, so a single measurement result is a square data matrix of dimension $n \times n$, where n is the number of electrodes. However, the diagonal of the matrix is not taken into account because it represents measurements with one electrode, which have no physical meaning. Therefore, a single measurement produces $N = n^2 - n$ values of electrical capacitance. An exemplary electrical capacitance tomography system is shown in Fig. 1. In this example, the excitation signal from module (3) is sent via the switches (2) to one of the electrodes mounted on the outer wall of pipe (1). This produces a signal proportional to the mutual capacitances on the other electrodes. These signals are amplified (4) and converted to digital (5). The switches (2) then reconnect the excitation (3) and amplifiers (4) to the next electrodes, one by one. Reconnections and measurements are repeated by signal control and measuring system (6) until the capacitance matrix is completed.

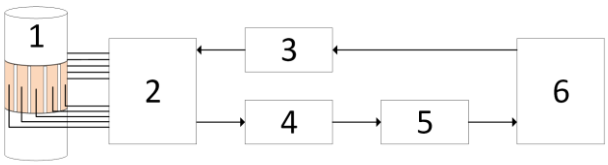

Fig. 1. Electrical capacitance tomograph: 1 – pipe with electrodes, 2 – switches, 3 – excitation, 4 – amplifiers, 5 – analog-to-digital converters, 6 – signal control and processing system.

The own-designed and built capacitance measurement system is based on the NEXYS-A7 digital circuit development platform, the main component of which is the XC7A100T-1CSG324C field-programmable gate array (FPGA) manufactured by Xilinx [19]. The block diagram of the capacitance sensor is shown in Fig. 2.

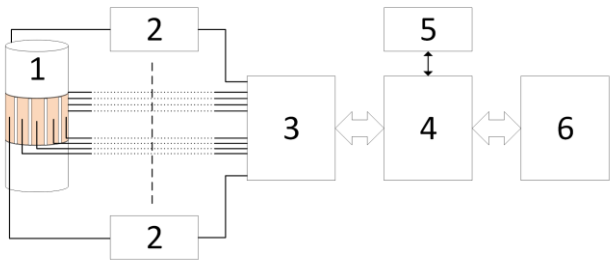

Fig. 2. Block diagram of the multi-electrode capacitance sensor: 1 – pipe with electrodes, 2 – ΔΣ modulators with excitation, 3 – LVDS interface, 4 – NEXYS-A7, 5 – local display, 6 – computer.

The NEXYS-A7 board (4 in Fig. 2) has a number of additional circuits that allow it to be used directly in a wide range of applications. For the multi-electrode capacitance sensor, two eight-bit input-output ports, a USB interface and a numeric display were used together with the graphic Pmod MTDS (Multi-Touch Display System) [20] add-on board (5). Moreover, the sensor set is supplemented with an original interface system of own design that is connected to two input-output ports and allows the connection of up to 16 measurement modules via LVDS (low-voltage differential signalling) interfaces (3). Eight identical measurement modules (2) were built as ΔΣ charge modulators capacitance-to-digital converters (CDC) and used in the research. The modulators were connected to eight electrodes mounted evenly around measuring pipe segment (1). Local display (5) can show current information, e.g. on actual capacitance values. The measured capacitance values are transmitted in real time to the computer (6) where they are stored and processed. Details of the used electronic components are summa-

Table 1. Electronic modules used to build the multi-electrode capacitance sensor.

No. in Figs. 2 & 4	Name	Manufacturer	Type	Specification
2	ΔΣ charge modulator capacitance to digital converter	own design and construction	–	sampling frequency 100–1200 kHz, output resolution 1bit, second order ΔΣ modulator
3	low-voltage differential signalling interface	own design and construction	–	16 channels, two transmission lines and one receiving line in each channel, maximum transmission frequency 400 MHz
4	digital circuit development platform	Digilent	NEXYS-A7	Artux-7 FPGA (clock >450 MHz), 129 MB DDR2 memory, USB, Ethernet, temperature sensor [19]
5	local display	Digilent	Pmod MTDS	2.8“ touchscreen display with QVGA resolution (320×240), PIC32MZ Microcontroller [20]

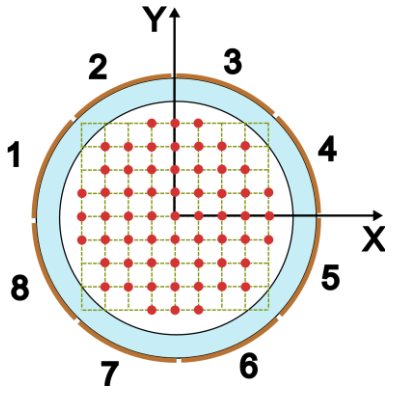

Fig. 3. Arrangement of electrodes in the test section: 1 to 8 – electrodes, XY – coordinate system. Red dots indicate 61 positions of the rod during reference measurements.

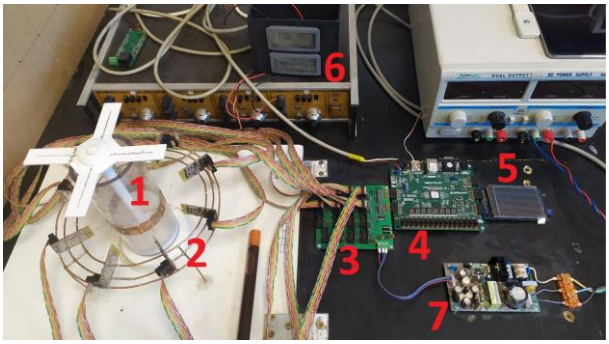

Fig. 4. Photograph setup: 1 – pipe with electrodes, 2 – ΔΣ modulators with excitation, 3 – LVDS interface, 4 – NEXYS-A7 FPGA, 5 – local display, 6 – 5 V power supply, 7 – +15 V and −15 V power supply of the capacitance sensor.

rized in Table 1. The arrangement of the measuring electrodes on the pipe wall in the test section is shown in Fig. 3 together with an XY coordinate system used in the subsequent discussion of tomograms.

A single measurement in the proposed device involves generating an excitation signal on one of the electrodes and simultaneously collecting responses on the remaining seven electrodes. This is followed by a program-controlled change of the excitation electrode. The complete measurement cycle requires eight partial measurements and returns 56 individual results for inter-electrode capacitances. The capacitance sampling frequency is 8 kHz, therefore a single measurement is done in 1 ms. At present, not all measurements are processed further and single measurements are transmitted once per second to the computer where they are written to a file. This is sufficient to analyze the stationary capacitance field in the test section.

A complete measuring system is shown in Fig. 4. Operation of the sensor set (No. 1 in Fig. 4) requires proper programming of the FPGA circuit (4). This includes the generation of signals necessary for the proper operation of ΔΣ modulators with excitation (2), i.e. reference clock signals with a frequency of 1.024 MHz, signals switching the modulator systems between the generation of the excitation signal and the capacitance measurement, and the collection and processing of digital outputs from the modulators. These signals are connected to ΔΣ modulators through an LVDS interface (3). Local display (5) is used for a quick overview of the sensor condition, e.g. actual capacitance values. For correct operation, the measuring system requires three supply voltages, which are provided by power supplies (6) and (7). The numbers 1 to 5 in Fig. 4 and in Fig. 2 showing the block diagram correspond to each other. In addition, the MicroBlaze soft-core microprocessor was programmed in the FPGA (4). The microprocessor is responsible for collecting the measurements and sending them to the cooperating computer. The FPGA software was created using the VIVADO Design Suite, while the program for the Microblaze microprocessor was written in the Xilinx Software Development Kit (SDK) environment.

3. Measurements

The constructed measuring system was installed on the wall of a polycarbonate pipe segment with an internal diameter of 60 mm and a wall thickness of 5 mm, Figs. 3 and 4. The pipe dimensions were selected to withstand the target operating conditions, i.e. temperature up to 70°C and pressure up to 4 bar. Eight electrodes mounted around the outer wall of the pipe were made of thin copper sheets measuring 20 mm × 25 mm. Two series of measurements were carried out. The first series was intended to generate reference data for reconstruction of the ca-

pacitance field, while the second one was intended to generate control data.

The reference data included 62 measurements of electrical capacity in the inter-electrode space: one measurement for an empty pipe and 61 measurements with a polyamide rod placed vertically in various locations relative to the longitudinal axis of the pipe, see Fig. 3. To define the position of the rod in the pipe cross-section, a rectangular grid was used with the origin in the pipe axis, grid size of 5 mm × 5 mm and a range from −20 mm to 20 mm. Some of the rod positions at the grid nodes were omitted because they were outside the pipe. The diameter of the rod was 12 mm and its relative permittivity was $\varepsilon_r = 3.6$.

The control data included a certain number of measurements, one for an empty pipe and the rest with a glass test tube filled with reservoir fluid and placed in different positions inside the pipe. The outer and inner diameter of the test tube was 15.5 mm and 13.3 mm, respectively. The relative permittivity of glass is $\varepsilon_r = 5.2$, while the relative permittivity of the reservoir fluid determined from the measurement of the change in the capacity of the air capacitor is $\varepsilon_r = 4.3$. Table 2 shows capacitances measured with the empty pipe. As expected, measured values are in the range from a tenth femtofarad to sub-picofarad.

4. Flow pattern reconstruction by artificial neural network

A neural network was used to analyze the collected data and generate tomographic images. A neural network consists of interconnected neurons, which are functions, most often non-linear, that convert the input signal. In the most commonly used networks, a neuron has *n* inputs and one output. Then, the weighted sum of *n* inputs is fed to the input of the function, and the output of the neuron is the result of the function. Neurons are stacked into layers, and the processed signals pass through subsequent layers of the neural network. The connections between the outputs and inputs of neurons, along with the weights assigned to them, are called synapses. Synapses also connect the outputs of the previous layer with the inputs of the next layer, with the first layer, the input layer, receiving the external input signals, and the last one, the output layer, generating the final result of the example neural network, Fig. 5.

The most important operation when creating a neural network is its training or learning procedure. To put it simply, it

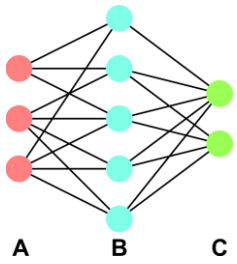

Fig. 5. Example neural network: A – input layer, B – hidden (internal) layer, C – output layer.

involves feeding a known signal to the input of a neural network and comparing the result of the network's operation with the expected one. Then, the synapse weights and sometimes the parameters of neuron functions are changed so that the result obtained is as close to the expected result as possible. This procedure is repeated many times for different sets of input and expected signals. A properly trained neural network produces correct results for all, or at least the vast majority, of the data sets used for training and, more importantly, can correctly process other similar input data.

The collected measurement data was processed using libraries written in Python. The sequential model in TensorFlow library with the Keras interface was used to generate and train the neural network [21]. The input data is a square matrix of dimension 8 with a zeroed diagonal, representing the measured capacitances between the sensor electrodes. The output is the coordinates of the polyamide test rod position. In order to simplify the neural network, the output data was written as a vector whose elements corresponded to specific positions of the rod, and detection of one specific position of the rod was assumed. The finally applied single neural network has the following structure:

- input layer of 64 neurons,
- hidden (internal) layer of 256 neurons,
- output layer of 2 neurons.

The designed neural network was subjected to a training process using model data normalized to the range from 0 to 1, after which it generated the correct result. The created single neural network was multiplied to detect all 61 standard positions of the rod, then all 62 partial neural networks were sequentially subjected to the training process and combined into one network

Table 2. Sample matrix of measured capacitances in pF.

		Measuring electrode							
		1	2	3	4	5	6	7	8
Excitation electrode	1		0.7428	0.0515	0.0736	0.1211	0.0750	0.1078	0.7246
	2	0.7260		0.6860	0.0305	0.1061	0.0781	0.1409	0.0461
	3	0.0408	0.6536		0.7132	0.0592	0.0718	0.1522	0.0936
	4	0.0774	0.0418	0.7009		0.6967	0.0278	0.1443	0.1007
	5	0.0869	0.0775	0.0481	0.8124		0.7047	0.0982	0.0925
	6	0.0781	0.0831	0.0829	0.0327	0.6167		0.6889	0.0440
	7	0.0338	0.0762	0.0883	0.0727	0.0509	0.6616		0.5091
	8	0.6815	0.0316	0.0796	0.0803	0.0920	0.0277	0.5540	

with the 8 × 8 input matrix and the output vector of 62 elements. An untypical structure of the neural network was forced by the low quantity of reference data, which caused problems with correct training of a single neural network.

The output of the neural network was used to generate a tomographic image of the flow patterns. For this purpose, pattern images corresponding to the pattern sensor outputs were prepared. Sample patterns assigned to position Y = −10 mm and X = −10 mm, −5 mm or 0 mm are shown, respectively, as A, B, C images in Fig. 6.

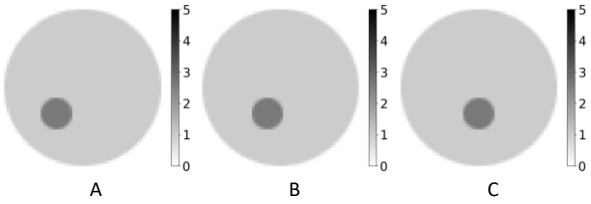

Fig. 6. Pattern tomographic images for three rod positions: A) X = −10 mm, Y = −10 mm; B) X = −5 mm, Y = −10 mm; C) X = 0 mm, Y = −10 mm.

The output of the network was a tomographic image, which was a weighted composite of the pattern images. In the first stage of checking the operation of the trained network, the pattern input data were reused and a practically accurate reproduction of the training data was received at the output, see Fig. 7, in which the rod positions correspond well with those in Fig. 6.

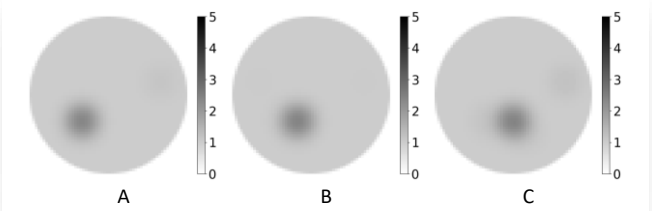

Fig. 7. Output tomographic images for three rod positions (shown in Fig. 6): A) X = −10 mm, Y = −10 mm; B) X = −5 mm, Y =−10 mm; C) X = 0 mm, Y = −10 mm.

5. Results

Measured data were statistically interpreted. Tables 3 and 4 show, respectively, the standard deviation and mean square deviation averaged from all measuring series for the full measuring matrix. It can be seen in Table 3 that the maximum value of the standard deviation equals 2.40 fF, the minimum value is 0.12 fF, and the average is 0.73 fF. Corresponding values for the mean square deviation in Table 4 are 2.18 fF, 0.10 fF and 0.75 fF. Table 5 shows absolute values of differences between capacitances measured with an empty pipe and one (typical) of the control measurements. For other control measurements, these values are similar. For the capacitance differences in Table 5, the corresponding maximum, minimum and average values are 22.82 fF, 0.68 fF and 8.48 fF.

More detailed analysis of the data presented in the tables leads to the conclusion that the average measured signal from

Table 3. Standard deviation of capacitance measurements in fF.

		Measuring electrode							
		1	2	3	4	5	6	7	8
Excitation electrode	1		0.9465	0.6765	0.1540	0.8125	1.1692	1.3954	0.8430
	2	1.2858		0.2860	0.2849	1.8582	0.2939	0.5941	1.3948
	3	1.0592	0.6496		0.2422	2.3983	0.2765	0.7954	0.5175
	4	1.1722	0.6917	0.8948		0.5086	0.3282	0.9162	0.4026
	5	0.7041	0.3241	0.3874	0.3495		0.3030	0.4687	0.7894
	6	0.6404	0.5667	0.8571	0.1727	0.9604		0.3967	0.6847
	7	2.0634	1.0953	0.1753	0.1232	0.4049	0.2758		0.3988
	8	1.0237	1.3063	0.8782	0.2486	0.4358	0.5352	1.2783	

Table 4. Mean square deviation of capacitance measures in fF.

		Measuring electrode							
		1	2	3	4	5	6	7	8
Excitation electrode	1		1.2879	0.5747	0.1293	0.6867	1.0652	1.2212	1.3083
	2	1.2172		0.3106	0.2402	1.8729	0.2571	0.5805	1.3344
	3	0.9432	1.0397		0.2072	2.1757	0.2502	0.8396	0.5796
	4	1.0591	0.9880	1.5000		0.5102	0.2795	0.8297	0.3988
	5	0.7558	0.3809	0.3352	0.6598		0.2650	0.4137	0.7610
	6	0.7116	0.5934	0.7754	0.1466	1.5413		0.3963	0.5763
	7	1.7749	0.9771	0.1639	0.1040	0.3774	0.2766		0.3470
	8	0.8583	1.2919	0.7816	0.2335	0.5941	0.4506	1.7812	

Table 5. Absolute value of differences between capacitance measures in fF.

		Measuring electrode							
		1	2	3	4	5	6	7	8
Excitation electrode	1		11.8022	0.6839	7.2696	21.7938	9.6818	4.6344	4.6308
	2	9.3650		1.4642	9.9730	20.4479	10.3518	8.5031	0.9020
	3	8.1539	10.8116		10.1570	22.5006	10.2041	8.4872	2.9265
	4	10.7341	9.6308	5.3480		2.1794	6.1330	9.7855	5.4407
	5	5.8758	6.1259	5.2418	14.4025		13.7443	9.9298	9.1028
	6	4.5810	2.9266	3.5715	4.2926	4.2589		10.2454	8.3952
	7	6.6521	4.9662	5.8284	1.6801	22.7186	17.8655		7.2578
	8	9.4027	9.2358	2.1333	3.0383	22.8179	7.7296	6.6307	

those presented in Table 5 is about 11 times greater than the noise represented in Tables 3 and 5, and varies from about 0.65 to 65. It might seem that these values are not very good but it should be noted that the average ε_r changes only by 25% when the filled glass test tube is inserted into the empty pipe. Moreover, the thickness of the pipe wall additionally decreases the system sensitivity to changes inside the pipe. The comparison of standard deviation or mean square deviation and the measurement range of 1 pF gives the average noise level at −63dB.

The prepared neural network was used for processing of control measurements. In this case, the test filled with reservoir fluid was used. Photographs in Fig. 8 show a few pipe and test tube configurations used to create control data for the reconstruction software. The images are aligned with the XY coordinate directions shown in Fig. 3. Figure 9 shows corresponding tomographic reconstructions. It can be seen in the tomographic images that the system reproduces correctly the real test tube location in the pipe cross-section.

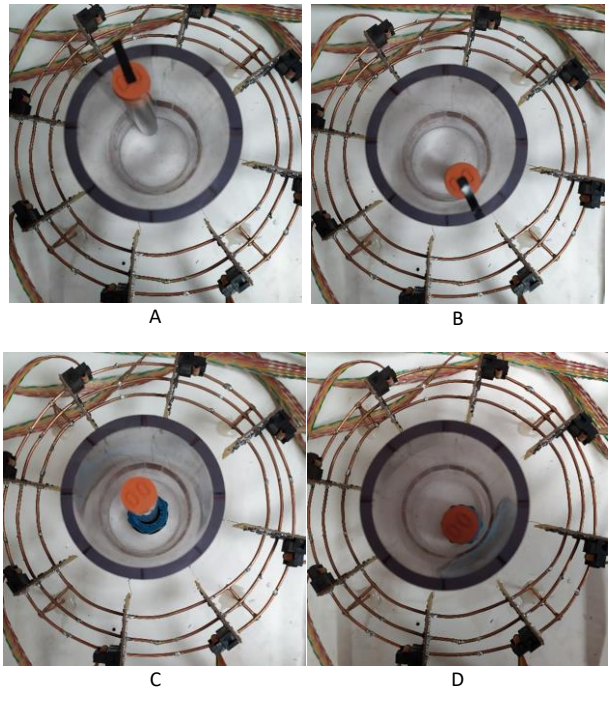

Fig. 8. Pictures of control pipe configurations with the test tube: A) close to electrode no. 2, B) close to electrode no. 6, C) close to the pipe centre, D) close to electrodes no. 5 and 6.

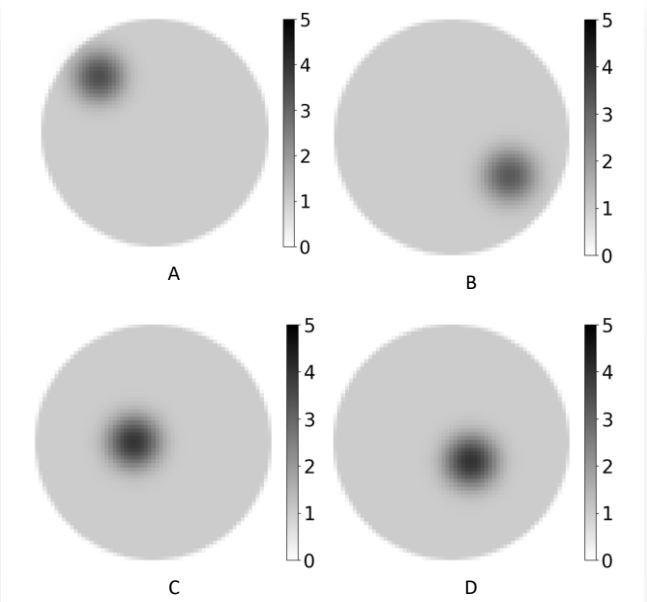

Fig.9. Output tomographic images of control pipe configurations shown in Fig. 8 with the test tube: A) close to electrode no. 2, B) close to electrode no. 6, C) close to the pipe centre, D) close to data electrodes no. 5 and 6.

6. Conclusions

The paper presents a novel eight-electrode capacitance meter designed to detect multiphase flow patterns in a medium with low permittivity, such as the reservoir fluid. Its operation was tested in laboratory conditions for static capacitance fields generated by introducing a polyamide rod or a glass test tube filled with reservoir fluid sample into the inter-electrode space.

The measurement system performed very well. The results were repeatable and had a good signal-to-noise ratio. The reconstruction of tomographic images in the case of data used to train the neural network was error-free, which confirms the selection of the appropriate structure of the neural network and the correctness of the training procedure. Reconstruction of target images with reservoir fluid also worked well. The position of the test tube was properly detected and the electrical permittivity was read at a noticeably higher level than in the case of data training the neural network. Both of these observations correspond to the actual measurement arrangement.

However, attention should be paid to the limitations of the proposed measurement system and the tomographic image reconstruction method. The use of only eight electrodes to measure capacitance significantly limits the accuracy and resolution of the reconstructed flow image. Moreover, the applied tomographic image reconstruction algorithm forces the detection of phase structures with a circular cross-section. For disturbances with a different shape, an approximation using a circle will be done. However, it should be expected that increasing the number of electrodes combined with more extensive training of the neural network should lead to better results.

Nevertheless, the designed capacitance meter has several significant advantages. The most important of them are a good signal-to-noise ratio and high sampling rate. The presented system can achieve signal-to-noise ratio of 63 dB at a sampling frequency of 1 kHz. For comparison, according to previous works, a generator-based two-electrode capacitance meters give signal-to-noise ratio of about 30 dB at a sampling frequency about 10 Hz. It should be noted that the capacitances measured here are very small, in the femtofarad range, which is difficult to measure accurately. Considering the above mentioned advantages, it should also be mentioned that the designed multichannel capacitance meter requires a specialized measuring system based on an expensive field-programmable gate array platform. The other meters can usually use commercially available integrated measurement circuits.

Acknowledgements

The research was supported by the third edition of the Programme of the Polish Ministry of Education and Science entitled "*Doktorat wdrożeniowy"* ("Industrial Doctoral Programme") − DWD/3/26/2019.

References

[1] Hu, X., Hu, S., Jin, F., & Huang, S. (Eds.) (2017). *Physics of Petroleum Reservoirs*. Petroleum Industry Press and Springer-Verlag. doi: 10.1007/978-3-662-53284-3

[2] Falcone, G., Hewitt, G.F., Alimonti, C., & Harrison B. (2002). Multiphase flow metering: current trends and future developments. *Journal of Petroleum Technology*, 54(4), 77–84. doi: 10.2118/74689-JPT

[3] Falcone, G., Hewitt, G.F., & Alimonti, C. (2009). *Multiphase Flow Metering*. Elsevier B.V.

[4] Thorn, R., Johansen, G.A., & Hjertaker, B.T. (2013). Three-phase flow measurement in the petroleum industry. *Measurement Science and Technology*, 24(1), 012003. doi: 10.1088/0957-0233/24/1/012003

[5] Hansen, L.S., Pedersen, S., & Durdevic, P. (2019). Multi-phase flow metering in offshore oil and gas transportation pipelines: trends and perspectives. *Sensors*, 19(9), 2184, doi: 10.3390/s19092184

[6] Meribout, M., Azzi, A., Ghendour, N., Kharoua, N., Khezzar, L., & AlHosani, E. (2020). Multiphase flow meters targeting oil & gas industries. *Measurement*, 165, 108111. doi: 10.1016/j.measurement.2020.108111

[7] *Roxar 2600 Multiphase Flow Meters*. Product Data Sheet RXPS-002516, Rev B (October 2022). Emerson Electric Co. https://www.emerson.com/ documents/automation/product-data-sheet-mpfm-2600-mvg-datasheet-roxar-en-us-170812.pdf [accessed 24 Nov 2023].

[8] Reinecke, N., & Mewes, D. (1996). Recent developments and industrial/research applications of capacitance tomography. *Measurement Science and Technology*, 7(3), 233−246. doi: 10.1088/0957-0233/7/3/004

[9] Rahman, N.A.Abd., Rahim, R.A, Nawi, A.M., Pei Ling, L., Pusppanathan, J., Mohamad, E.J., Seong, C.K., Din S.M., Ayob, N.M.N., & Yunus, F.R.M. (2015). A review on electrical capacitance tomography sensor development. *Jurnal Teknologi (Sciences & Engineering)*, 73(3), 35–41. doi: 10.11113/jt.v73.4244

[10] Yang, W.Q., & Peng, L. (2003). Image reconstruction algorithms for electrical capacitance tomography. *Measurement Science and Technology*, 14(1), R1–R13, doi: 10.1088/0957-0233/14/1/201

[11] Rasel, R.K., Shah, M., Chowdhury, S.M., Marashdeh, Q.M., & Teixeira, F.L. (2022). Review of selected advances in electrical capacitance volume tomography for multiphase flow monitoring. *Energies*, 15(14), 5285. doi: 10.3390/en15145285

[12] Nooralahiyan, A.Y., Hoyle, B.S., & Bailey N.J. (1994). Neural network for pattern association in electrical capacitance tomography. *IEE Proceedings – Circuits, Devices and Systems*, 141(6), 517–521. doi: 10.1049/ip-cds:19941190

[13] Marashdeh, Q., Warsito, W., Fan, L.S., & Teixeira F.L. (2006). A nonlinear image reconstruction technique for ECT using a combined neural network approach. *Measurement Science and Technology*, 17(8), 2097−2103. doi: 10.1088/0957-0233/17/8/007

[14] Flores, N., Kuri-Morales, A., & Gamio, C. (2006). An application of neural networks for image reconstruction in electrical capacitance tomography applied to oil industry. In *Progress in Pattern Recognition, Image Analysis and Applications*" (pp. 371–380). *Proceedings of the 11th Iberoamerican Congress on Pattern Recognition*, CIARP 2006, 14–17 November, Cancún, Mexico. Springer-Verlag, doi: 10.1007/11892755

[15] Chen, X., Hu, H., Liu, F.& Gao, X.X. (2011). Image reconstruction for an electrical capacitance tomography system based on a least-squares support vector machine and a self-adaptive particle swarm optimization algorithm. *Measurement Science and Technology*, 22(10), 104008. doi: 10.1088/0957-0233/22/10/104008

[16] Wang, H., Hu, H., Wang, L., & Wang, H. (2012). Image reconstruction for an Electrical Capacitance Tomography (ECT) system based on a least squares support vector machine and bacterial colony chemotaxis algorithm. *Flow Measurement and Instrumentation*, 27, 59–66. doi: 10.1016/j.flowmeasinst.2012.05.006

[17] Chen, X., Hu, H., Zhang, J. & Zhou, Q., (2012). An ECT system based on improved RBF network and adaptive wavelet image enhancement for solid/gas two-phase flow. *Chinese Journal of Chemical Engineering* 20(2), 359–367. doi: 10.1016/S1004-9541(12)60399-1

[18] Xu, Z., Wu, F., Yang, X., & Li Y. (2020). Measurement of gas-oil two-phase flow patterns by using CNN algorithm based on dual ECT sensors with Venturi tube. *Sensors*, 20(4), 1200. doi: 10.3390/s20041200

[19] *Nexys A7 FPGA Board Reference Manual*, Revised July 10, 2019. Digilent Inc. https://digilent.com/reference/programmable-logic/nexys-a7/reference-manual [accessed 24 Nov. 2023].

[20] *Pmod MTDS Reference Manual*. Digilent Inc. https://digilent.com/reference/pmod/pmodmtds/reference-manual [accessed 24 Nov. 2023].

[21] *TensorFlow Core Guide – The Sequential model*. TensorFlow. https://www.tensorflow.org/guide/keras/sequential_model [accessed 24 Nov. 2023].